Energieforschungsprogramm

Publizierbarer Endbericht

Programmsteuerung:
Klima- und Energiefonds

Programmabwicklung:
Österreichische Forschungsförderungsgesellschaft mbH (FFG)

Endbericht
erstellt am
27/02/2026

Projekttitel:
AM4CO2 - Additive Manufacturing von CO2-Behältern

Projektnummer: 915029

Ausschreibung	XX. Ausschreibung Energieforschungsprogramm
Projektstart	01/09/2024
Projektende	30/11/2025
Gesamtprojektdauer (in Monaten)	15 Monate
ProjektnehmerIn (Institution)	RHP-Technology GmbH
AnsprechpartnerIn	DI Dr. Erich Neubauer
Postadresse	Forschungs- und Technologiezentrum A-2444 Seibersdorf, Austria
Telefon	+43 (2255) 20 600
Fax	+43 (2255) 20 600
E-mail	e.ne@rhp.at
Website	rhp.at

AM4CO2

Additive Manufacturing von CO2-Behältern

AutorInnen:
Carlos Belei
Emanuel Feuerstein
Enrique Ariza
Erich Neubauer

1 Inhaltsverzeichnis

2 Einleitung

2.1 Aufgabenstellung

The objective of this project was to evaluate the suitability of additive manufacturing—specifically Plasma Metal Deposition (PMD)—for producing components relevant to CO_2-transport infrastructure. The work focused on identifying and assessing material systems that can withstand the mechanical and corrosive conditions associated with CO_2 pipelines and pressure vessels. This included selecting promising steel and non-steel alloys, establishing PMD process parameters for these materials, and characterizing the resulting microstructure, mechanical properties, and corrosion behavior under CO_2-relevant conditions.

A further goal was to demonstrate the applicability of PMD for industrially relevant geometries through the design, fabrication, and testing of representative demonstrator components. These demonstrators were produced using a hybrid manufacturing approach combining additive and conventional processes. In addition, the project aimed to quantify the energy consumption of PMD and compare it to traditional manufacturing routes, thereby assessing the potential ecological and economic benefits of additive manufacturing for CO_2-transport applications.

2.2 Schwerpunkte des Projektes

Traditional manufacturing methods such as rolling and forging are widely used for producing pipes and tanks for CO_2 transport. While these processes are efficient for large-scale production of standard components, they normally offer limited flexibility when complex geometries are required (see Figure 1). They also often demand extensive post-processing to meet final specifications. In contrast, additive manufacturing (AM) provides significant design freedom, enabling the creation of intricate shapes with high precision and reduced need for rework. This makes AM particularly attractive for CO_2-transport applications, where optimized geometries can improve performance and reduce costs.

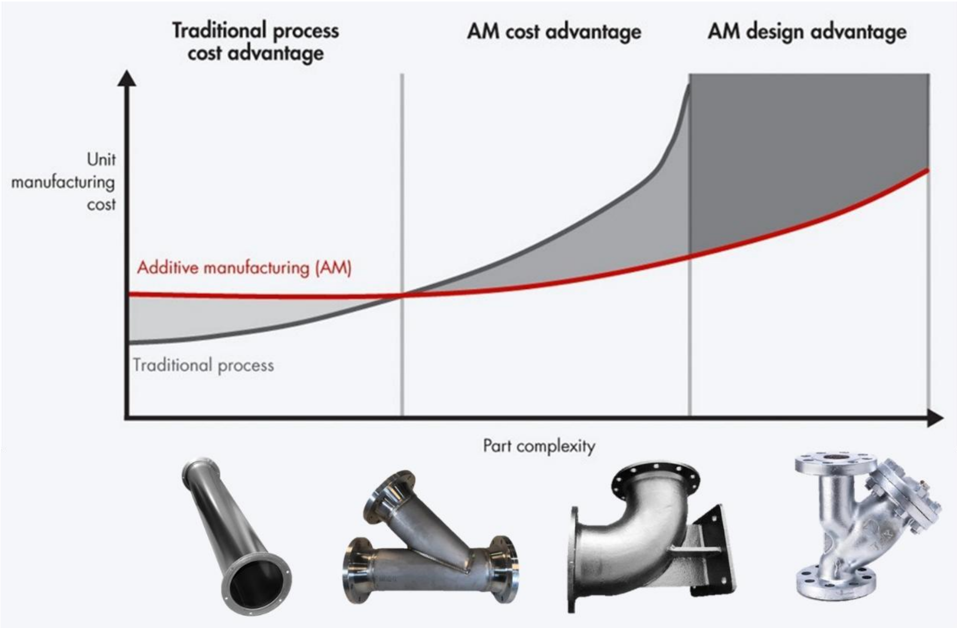

Figure 1 – Relationship between cost and complexity for additive manufacturing and conventional processes. Adapted from [1]

AM also allows the use of advanced materials that are otherwise expensive or difficult to process conventionally. Titanium and Scalmalloy® are notable examples, offering excellent corrosion resistance (an essential property for CO_2 pipelines and pressure vessels, especially in areas prone to flow-induced corrosion). Furthermore, AM enables near-net-shape production, minimizing material waste and machining time. Hybrid approaches that combine conventional forming with AM — such as printing flanges onto pre-formed pipes — further expand the range of possible solutions. Figure 2 sumarizes the main advantages of AM for different application scenarios regarding component geometry.

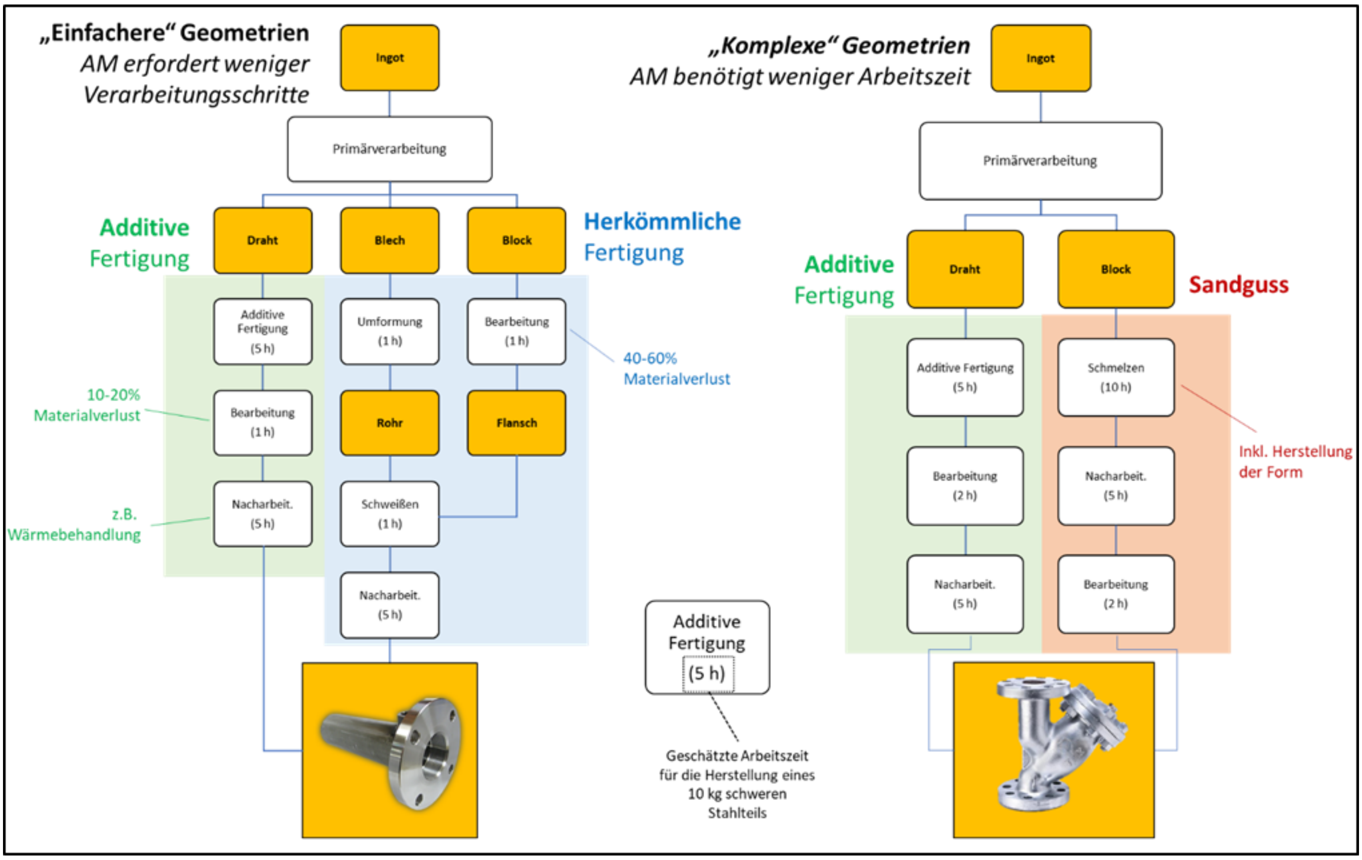

Figure 2 – Comparison between additive manufacturing and conventional manufacturing processes currently used for CO_2 transport components

Despite these advantages, the use of AM for CO_2 transport and storage infrastructure remains largely unexplored. Significant knowledge gaps exist regarding both process capabilities and material behavior in this specific application. Addressing these gaps forms the core motivation of the project: to investigate the opportunities and limitations of AM for developing efficient, safe, and innovative CO_2-transport components.

Since the work deals with materials and manufacturing processes for CO_2-transport components, environmental and economic goals are closely linked: reducing energy consumption directly lowers production costs and increases profitability. The project therefore sets quantitative targets such as achieving a 30% reduction in energy use compared to conventional manufacturing, improving corrosion resistance of non-steel components by 20%, and reducing component weight by 20% without compromising performance.
These goals are grounded in the advantages of additive manufacturing, particularly its near-net-shape capability, reduced material waste, and suitability for advanced corrosion-resistant materials like titanium or specialized aluminum alloys.

2.3 Einordnung in das Programm

The project aligns with the *Energieforschungsprogramm – XX. Ausschreibung* by addressing key technological challenges in the decarbonisation of energy-intensive infrastructure. By developing additively manufactured CO_2-transport components with reduced energy and material demand (in this case via AM), with improved corrosion resistance, and (potentially) lower structural mass, the project directly contributes to the program goals of increasing energy efficiency, reducing greenhouse-gas emissions, and enabling climate-neutral industrial systems. Moreover, the focus on advanced materials, near-net-shape manufacturing, and hybrid production routes supports the call emphasis on innovative, resource-efficient technologies that strengthen Austria's capability to build resilient and sustainable energy infrastructure. This therefore fits specifically *Ausschreibungsschwerpunkt 4: Klimawandelanpassung der Energieinfrastruktur*.

2.4 Verwendete Methoden

The project employed a comprehensive methodological approach covering material selection, additive manufacturing, characterization, and demonstrator validation. The work began with an extensive literature review to define material requirements for CO_2-transport components and to identify suitable alloy systems. Candidate materials were evaluated based on mechanical performance, corrosion resistance, and processability, and grouped into steel and non-steel categories.

Additive manufacturing was carried out using the Plasma Metal Deposition (PMD) process. For each selected material, key process parameters were optimized, and wall structures were produced to generate test coupons. The subsequent material characterization included microstructural analysis to assess phase distribution and defect formation, tensile testing to determine mechanical properties, and corrosion testing under CO_2, H_2O, and combined CO_2+H_2O atmospheres at temperatures and pressures representative of CO_2-transport conditions.

Based on the characterization results, one steel and one non-steel alloy were selected for demonstrator fabrication. Demonstrators were designed according to manufacturing constraints and application-relevant geometries. Their production followed a hybrid manufacturing route combining PMD deposition, subtractive machining, and welding of commercial flanges. Pressure testing was performed to replicate mechanical loads encountered in CO_2-transport pipelines. Finally, the energy consumption of the PMD process was quantified for the selected materials and geometries and compared to conventional manufacturing routes such as casting and machining.

2.5 Aufbau der Arbeit

The report is structured to reflect the technical development path of the project. Following the introduction and definition of the project objectives, the theoretical background is presented, including material requirements for CO_2-transport applications and an overview of relevant manufacturing technologies.

The methodological framework is then outlined, followed by a detailed description of the individual project steps: material screening, PMD process development, material characterization, selection and design of demonstrators, manufacturing, and pressure testing. The subsequent chapter presents the results of each step and discusses their implications with respect to the project goals.

The report concludes with an evaluation of the PMD energy expenditure in comparison to conventional manufacturing processes, followed by a summary of the key findings and an outlook on future developments and potential industrial applications.

3 Inhaltliche Darstellung

The work was comprised by the following sequential steps:

1. Literature research and candidate selection

Goal was to identify material requirements and suitable alloy systems, and select the most promising candidates based on performance and processability. The selection was categorized in two groups: steel and non-steel alloys, with three candidates selected for each.

2. Investigation of 3D printing via Plasma Metal Deposition (PMD)

The feasibility of PMD was evaluated and key process parameters were optimized for the selected materials. Walls were produced, from which coupons were extracted.

3. Material characterization

A systematic material characterization was performed to assess structural integrity and functional performance. Comprised of:

   a. *Microstructural analysis:* to evaluate phase distribution, grain structure, and potential defects;
   b. *Tensile testing:* to determine strength and ductility properties (i.e. mechanical performance);
   c. *Corrosion testing:* assessed under CO_2, H_2O, and combined CO_2+H_2O atmospheres, at temperature and pressure conditions similar to what is currently used for CO_2 transportation purposes.

4. Material selection for the demonstration (upscaling)

The most suitable material from each category (steel and non-steel) was selected based on the overall performance results for demonstrator fabrication.

5. Design of demonstrators

Demonstrator components were designed considering manufacturing constraints, operational requirements, and representative geometries for CO_2 transportation applications.

6. Manufacturing of demonstrators

The demonstrators were manufactured according to the finalized design using a hybrid approach, combining additive and subtractive processes, as well as welding of similar and dissimilar materials. Consisted of two main stages:

a. *3D printing via PMD:* using parameters and strategies learned from earlier project stages;
b. *Welding of commercial flanges:* commercially available flanges were procured and welded to the 3D-printed vessels demonstrators.

7. Pressure testing of demonstrators

Performed as a means to replicate the mechanical loads experienced by the pipelines on CO_2 transportation conditions.

8. Assessment of energy expenditure of PMD for the selected materials/geometries

The energy consumption of the PMD process was evaluated for the selected materials and geometries. These results were then compared to traditional manufacturing routes such as casting and machining.

Respective results from each of these project steps are presented in the following chapter.

4 Ergebnisse und Schlussfolgerungen

4.1 Literature research and candidate selection

Literature research was conducted based on a set of pre-requisites concerning materials to be used in CO_2 transportation pipelines. According to [2–4], the main pre-requisites are as follows:

1. CO_2 dissolves in liquid water and forms carbonic acid, causing corrosion;
2. Rapid depressurization can expose materials to sub-critical temperatures (down to −60 °C);
3. Sufficient base-material toughness is required to arrest ductile-fracture propagation;
4. Supercritical CO_2 has strong solvent properties that must be considered.

The project focused on the mechanical and corrosion-related aspects of CO_2 exposure (items 1 and 3), where material behavior is most critical for our objectives. Although points 2 and 4 are also relevant in a broader CO_2-handling context, they extend beyond what this work can realistically address within its current boundaries.

Accordingly, six commercial alloys were selected for evaluation. These are materials that are either not currently used or only minimally used in CO_2 transportation pipelines/reservoirs. The group was divided into ferrous (steel) and non-ferrous alloys. For the ferrous category, the intention was to include one conventional, widely used steel as a reference point, along with two high-performance steels that are less commonly applied in this context. For the non-ferrous category, the focus shifted toward high-performance alloys that are well established in other engineering sectors but have not yet been adopted for CO_2 transport. The selected candidates, along with the rationale behind their inclusion, are outlined below.

Ferrous alloys:

- Stainless steel 316L (EN 1.4404): A widely used engineering stainless steel. Rarely applied in CO_2 systems due to its higher cost and often unnecessary performance margin. Used here as a baseline for comparison with the other two alloys.
- Duplex stainless steel 2209 (AWS A5.9 | ISO 14343): Selected as a representative duplex grade offering higher strength than standard austenitic steels and good CO_2-environment corrosion resistance. Included to benchmark how a mid-range, widely used duplex alloy performs under the test conditions.
- Super-Austenitic stainless steel SAFUREX™ (EN 1.4477): Chosen for its very high corrosion resistance and mechanical strength, making it a premium candidate for demanding environments. Serves as the high-performance reference within the ferrous alloy group.

Non-ferrous alloys

- Inconel 718: Chosen for its excellent high-temperature strength and outstanding corrosion resistance in acidic and CO_2-rich environments. Serves as a robust, high-performance candidate for demanding conditions.
- Ti-6Al-4V: Selected due to its high specific strength and proven corrosion resistance in aqueous and CO_2 environments. Included as a lightweight, well-established engineering alloy with strong performance potential.
- AlMgSc (Scalmalloy™): Included as a representative high-strength aluminum alloy commonly used in AM applications. Evaluated to determine whether its low density and good mechanical properties could translate to CO_2-related service, despite aluminum's known sensitivity to acidic environments.

4.2 3D-printing

The selected alloys were procured in the wire form and processed via Plasma Metal Deposition (PMD®), a plasma-based, directed-energy deposition additive manufacturing technique. Schematics of the process are presented in Figure 1.

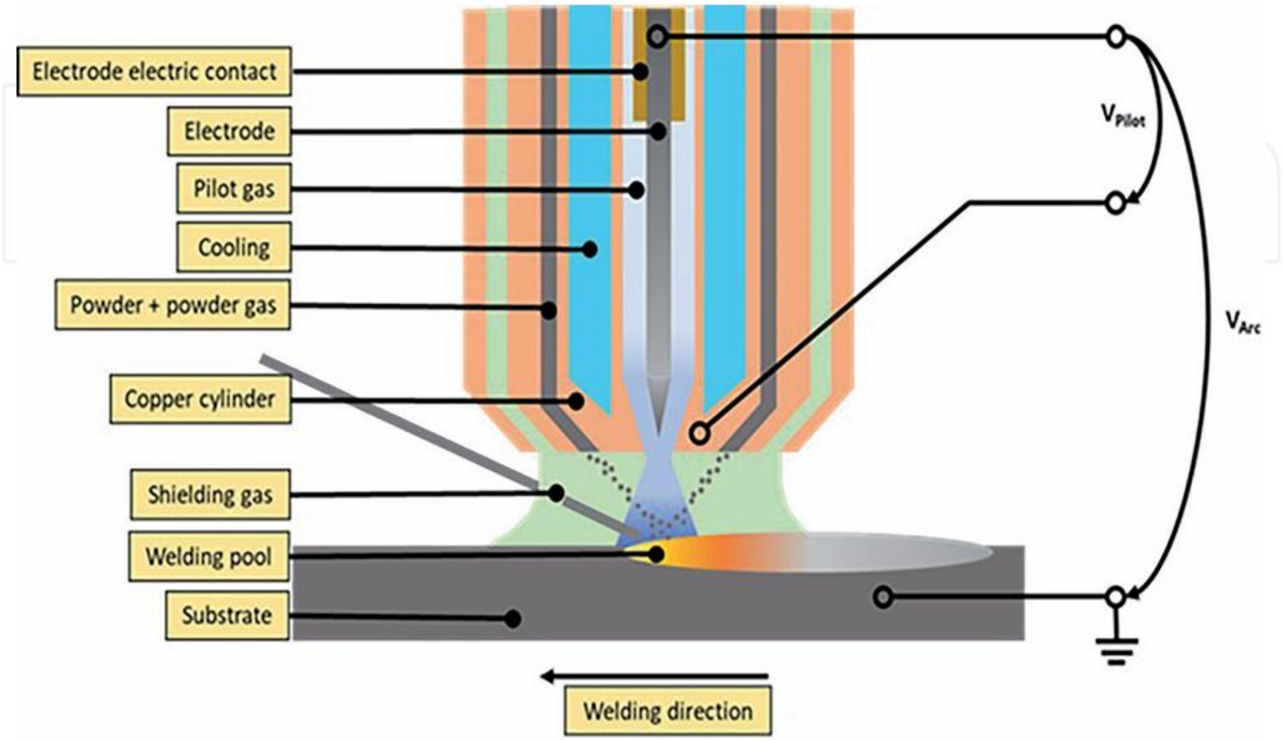

Figure 3 – Schematics of the Plasma Metal Deposition process [5]

For the sake of the material evaluation, 3D printed walls with minimum dimensions of 100 mm (l), 60 mm (h) and 6 mm (w) were produced. An overview of the produced walls is shown in Figure 4.

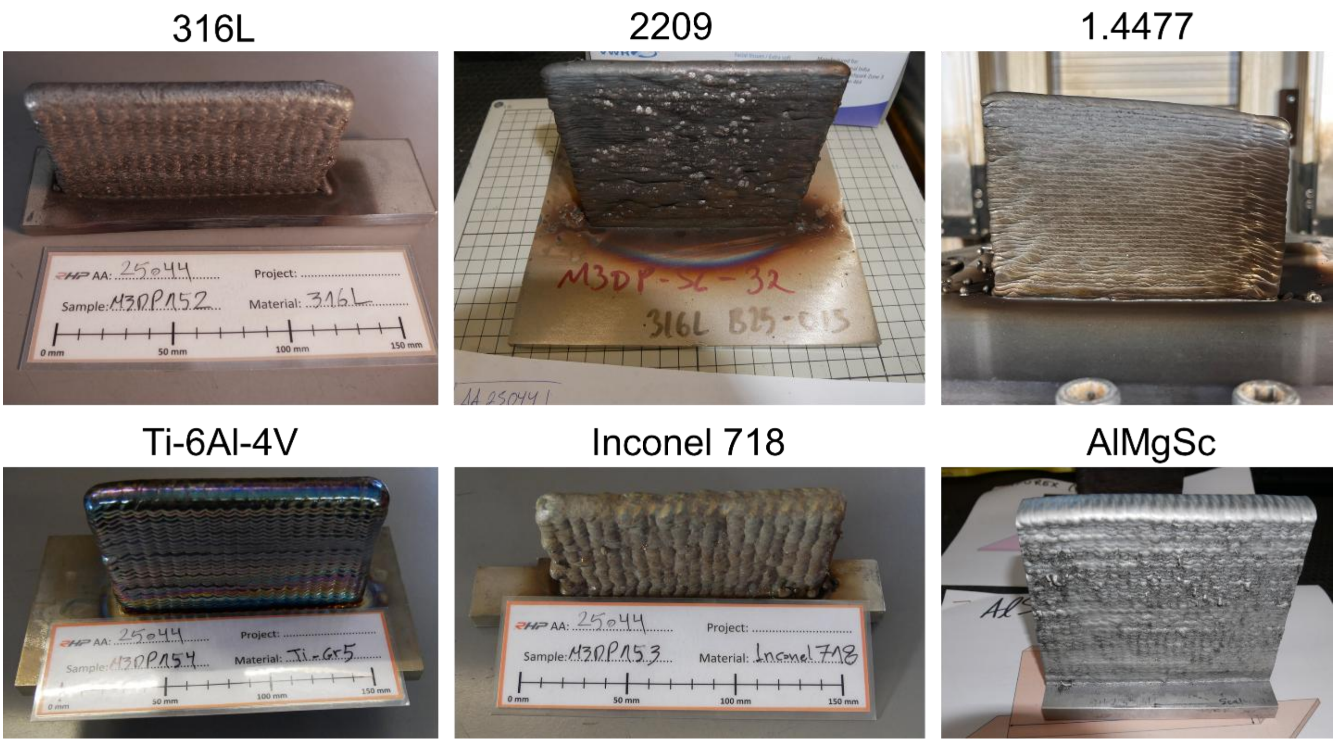

Figure 4 – Overview of test walls produced via PMD during the project

From each of these walls, samples for CO2 corrosion tests (5 x 5 x 5 mm cubes), tensile tests (see ASTM E8 for PM products) in both horizontal and vertical directions and microstructure (cross-section) were extracted via Electrical Discharge Machining (EDM). Results are described in the following sub-sections.

4.3 Microstructural analysis

Figure 5 presents the macrostructures of the three 3D-printed ferrous alloys. In alloy 1.4477, fully columnar grains 10–20 mm in length developed parallel to the build direction. Alloy 316L showed the same epitaxial solidification behavior, though with shorter columnar grains of approximately 2–3 mm. In contrast, the 2209 wall exhibited epitaxial grains that grew preferentially at an angle of about 45° relative to the printing direction, rather than strictly vertically. Moreover, the 316L sample specifically has noticeable lack of fusion pores, which suggests a colder process and could therefore be improved with a deeper parameter optimization step.

Figure 5 – Cross-sections of the steels produced via PMD. From left to right: 316L, 2209, 1.4477

Microstructure differed between the different steels (Figure 6). In fully austenitic 316L, the dendritic solidification structure is clearly revealed due the HCl–H_2O_2 etchant preferentially dissolving the interdendritic regions, which are less corrosion-resistant than the dendrite cores. In the duplex and super-duplex steels (2209 and 1.4477), a characteristic Widmanstätten morphology is observed, where austenite laths nucleate at δ/γ interfaces and grow into the ferrite grains [6,7].

Owing to the very high cooling rate (~10^2 K/s), this transformation is incomplete: instead of forming continuous laths, the austenite appears fragmented into discontinuous plates and massive secondary austenite (γ_2). This γ_2 forms because rapid cooling suppresses diffusion-controlled austenite growth, freezing in compositional gradients and promoting intragranular nucleation rather than coherent Widmanstätten plates [7–9].

Based on color threshold segmentation performed on microstructural pictures, the volumetric ratio between ferrite and austenite in the 2209 and 1.4477 steels was estimated at 31%:69% and 48%:52%, respectively.

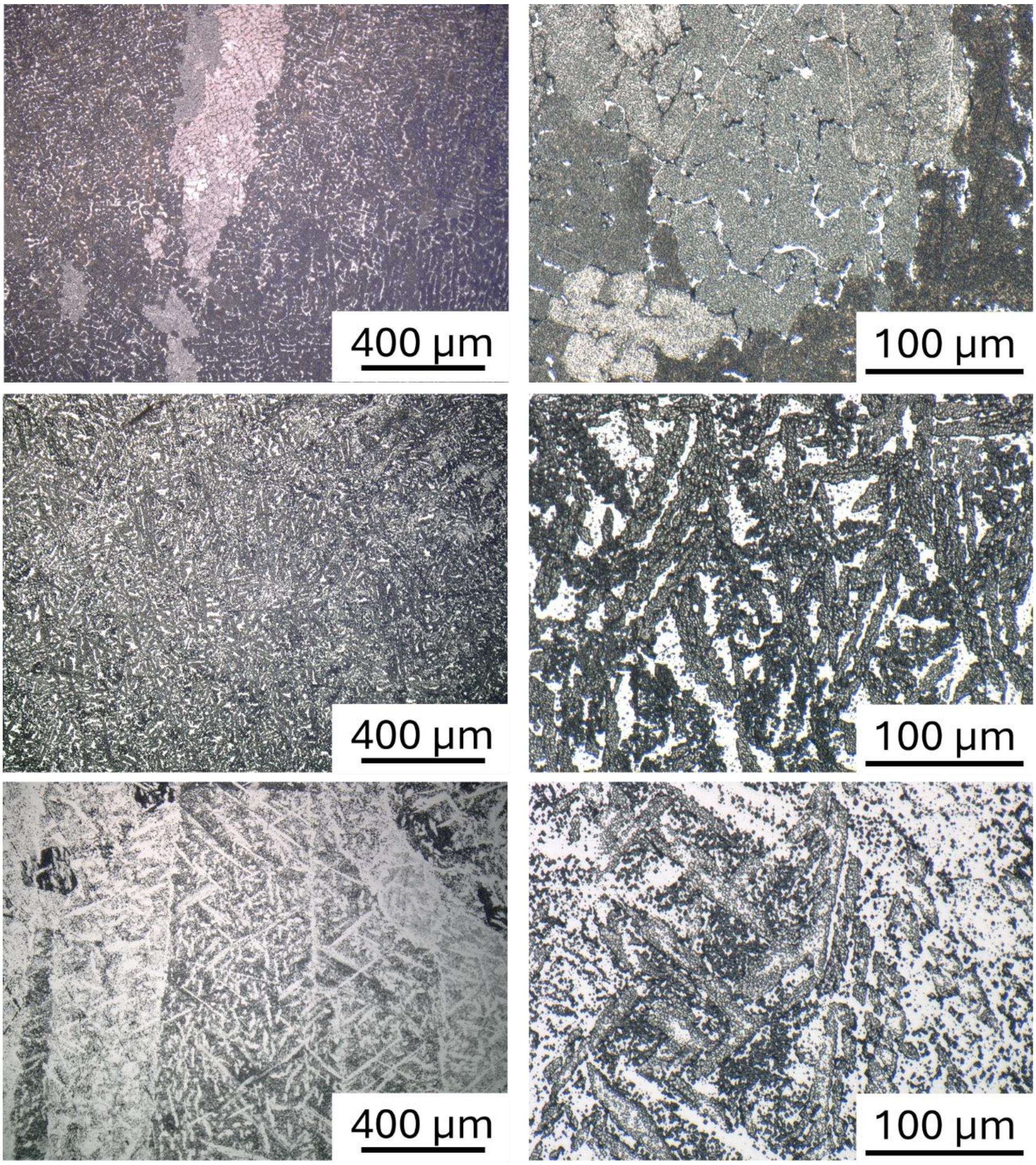

Figure 6 – Microstructures found on the steels produced via PMD. From top to bottom: 316L, 2209, 1.477. Left column: 200x magnification; Right: 500x

On the macrographs from non-ferrous alloys (Figure 7), Ti-6Al-4V shows a relatively coarse grain structure, with grains of approximately 100–200 µm that appear quasi-equiaxed at low magnification; however, the layer-by-layer deposition is still evident through the visible banding.

In718 by contrast develops the expected elongated columnar grains that grow at a slight inclination relative to the build direction, extending over several millimeters. For the Al-Mg-Sc alloy, the grain size is so fine that individual grains cannot be resolved in the macrograph; instead, the dominant visible feature is the layer transition itself, which appears as faint tonal variations corresponding to the thermal cycling between successive passes.

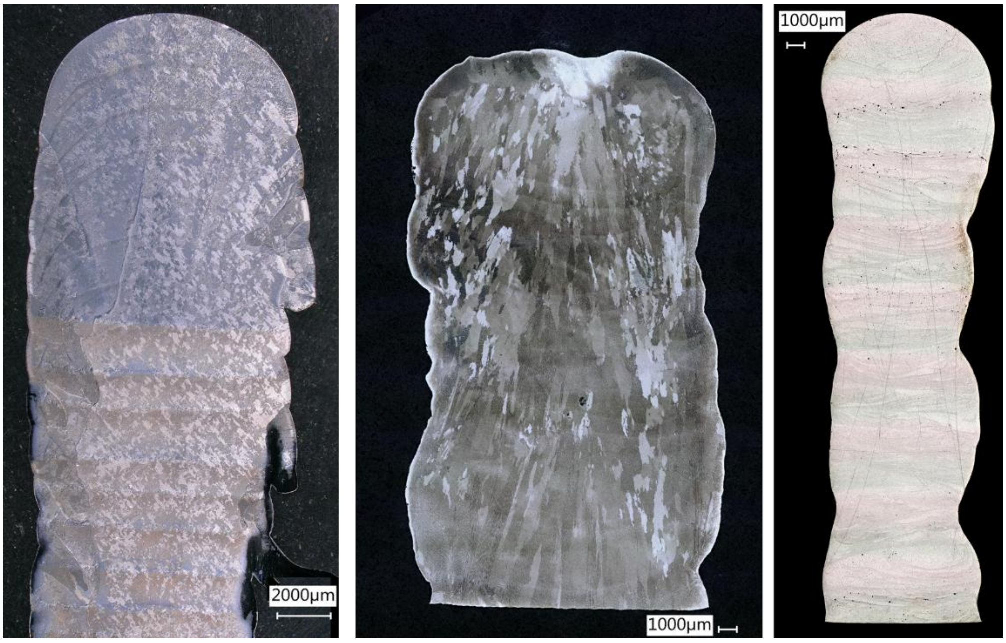

Figure 7 - Cross-sections of the non-steel alloys produced via PMD. From left to right: Ti-64, In718, AlMgSc

In the microstructure (Figure 8), Ti-6Al-4V shows the expected Widmanstätten $\alpha+\beta$ morphology formed during cooling from the prior-β phase [10]. In718 exhibits a heterogeneous, island-like γ matrix with a faint dendritic or cellular appearance, most likely caused by Nb- and Mo-rich microsegregation, which produces interdendritic Laves-type regions during solidification [11,12]. The Al-Mg-Sc alloy is dominated by Al_3Sc-based precipitates [13,14] decorating grain boundaries and triple junctions; most particles fall in the 1–2 µm range, with occasional coarsened precipitates reaching ~10 µm due to localized thermal exposure.

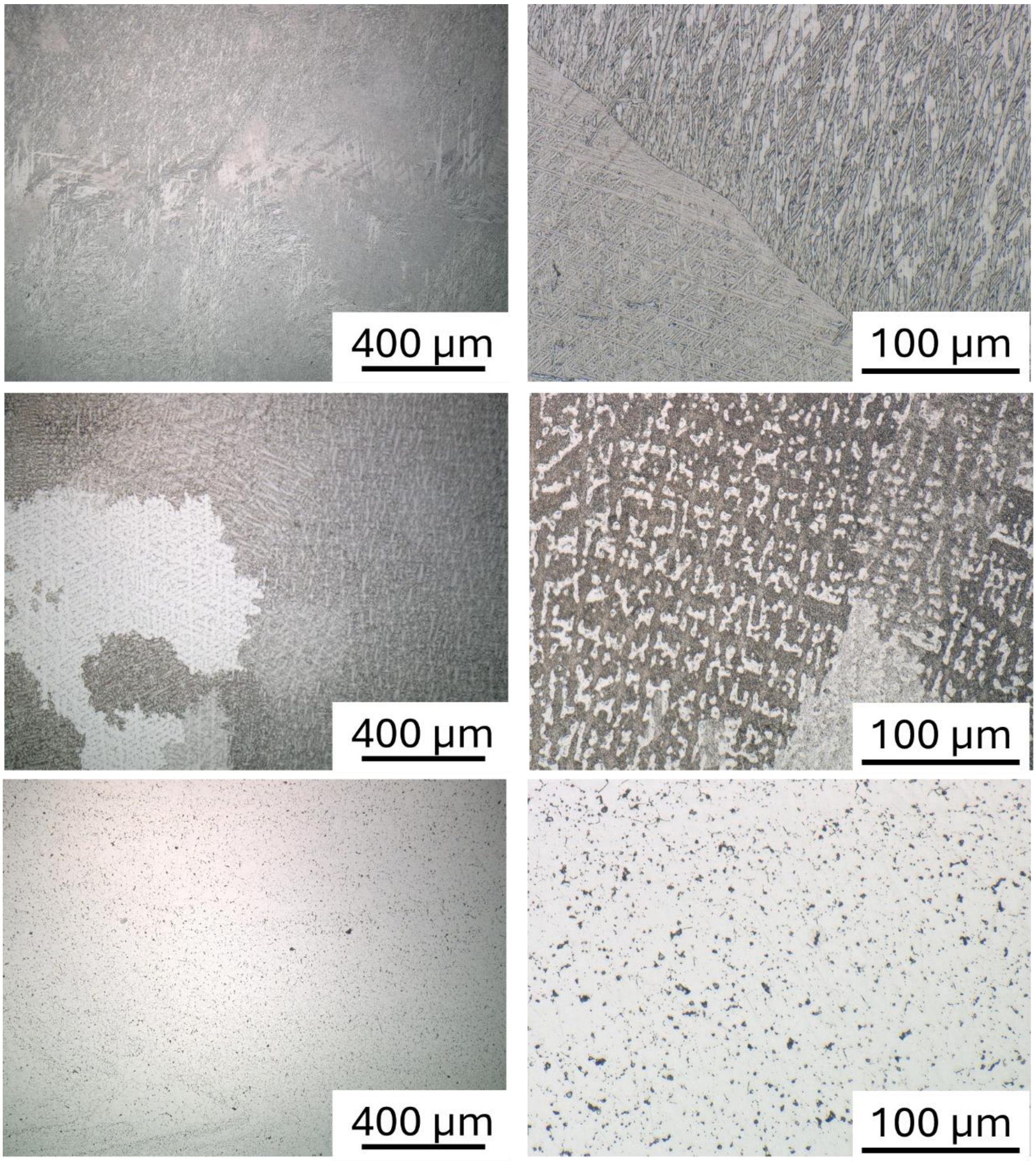

Figure 8 - Microstructures found on the non-steels produced via PMD. From top to bottom: Ti-64, In718, AlScMg. Left column: 200x magnification; Right: 500x

4.4 Tensile tests

Tensile tests were conducted on samples extracted from each 3D-printed wall, in horizontal and vertical directions. The summary of the average measured values is presented in Table 1. AlMgSc and Ti-6Al-4V were also heat treated after printing. AlMgSc: 520 °C (1h), quenched in water, 300 °C (4h), cooled in oven; Ti-6Al-4V: 700 °C, 24 h, cooled in oven.

Table 1 – Summary of mechanical properties as measured via tensile testing

Material	Orientation	Condition	E-Modul [GPa]	St.dev [GPa]	σ_y [MPa]	St.dev [MPa]	UTS [MPa]	St.dev [MPa]	EaB [%]	St.dev [%]
316L	H	as-printed	113,0	10,7	338,3	5,6	613,5	20,7	41,6	7,3
316L	V	as-printed	70,6	19,9	327,8	16,9	592,9	9,3	47,5	5,0
1.4477	H	as-printed	146,6	24,5	625,8	11,0	876,3	44,7	30,5	2,8
1.4477	V	as-printed	155,1	4,2	581,3	8,8	853,7	9,6	39,6	2,5
2209	H	as-printed	133,7	16,0	454,4	10,9	793,0	16,4	45,8	4,8
2209	V	as-printed	153,4	9,6	450,1	7,4	792,3	24,1	51,7	7,9
Ti-64	H	as-printed	113,9	2,9	877,5	24,3	959,3	21,1	8,3	1,6
Ti-64	V	as-printed	108,3	1,9	827,4	22,3	903,7	20,0	4,7	0,8
Ti-64	H	HT	115,5	1,7	900,4	14,3	974,6	14,9	8,0	1,4
In718	H	as-printed	129,5	35,3	416,1	27,2	667,8	50,3	24,0	17,5
In718	V	as-printed	113,5	57,4	464,5	107,7	828,0	68,3	35,7	11,2
AlMgSc	H	as-printed	55,5	20,6	275,4	7,0	450,0	4,8	28,1	5,5
AlMgSc	V	as-printed	58,1	24,8	279,1	6,6	452,1	13,4	26,5	4,8
AlMgSc	H	HT	58,3	21,1	280,9	42,3	473,0	34,7	33,4	1,1
AlMgSc	V	HT	52,8	3,9	273,9	20,7	322,4	85,4	6,9	4,7

Other than the commonly printed alloys like Ti-6Al-4V and 316L, the remaining materials can also be processed via PMD and still achieve reasonable properties. Compared with their wrought, annealed counterparts, the as-printed AM-PMD results vary, as shown in Figure 9. Alloys such as AlMgSc, 2209, and In718 exhibit notably higher elongation, with only a small reduction in yield strength in the first two. For the other materials, the wrought versions remain slightly stronger and more ductile. Some alloys (particularly 316L and In718) also show significantly lower elastic modulus values, which can be directly linked to large lack-of-fusion voids.

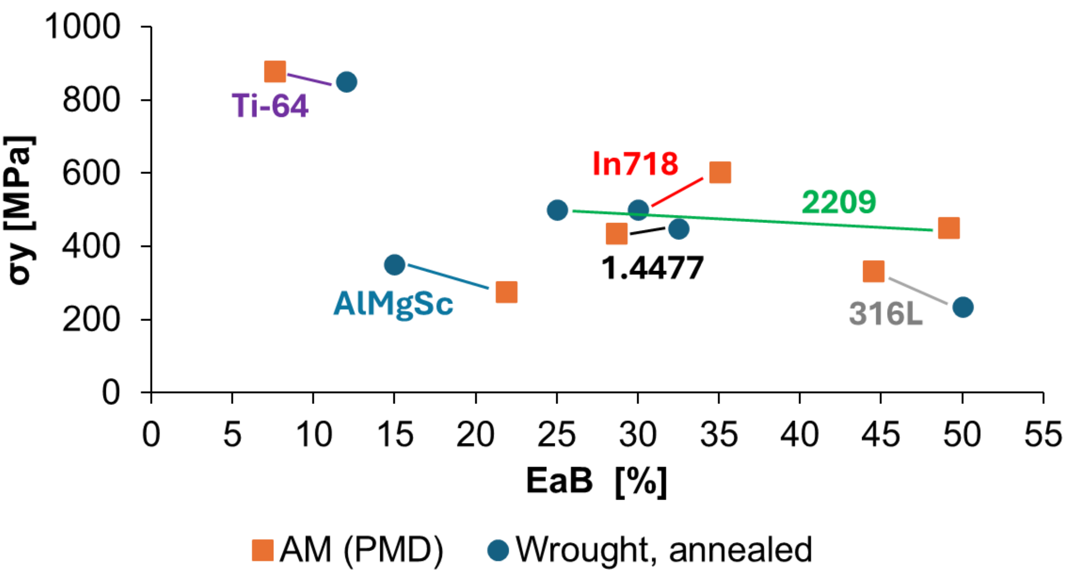

Figure 9 – Overview of the comparison between PMD materials and their wrought counterparts

4.5 Corrosion tests

Corrosion tests were performed according to the schematics provided in Figure 10-a. Due to the high cost in acquiring specialized reactors for such test, three custom-made components out of stainless steel 304 were produced, in which a POM tube was inserted. Inlet and outlet channels were added to the cap, which is screwed into the main reactor body. Figure 10-b shows the final results. These vessels were successfully pressure tested with water at 120 bar for 10 minutes (setup shown in **Error! Reference source not found.**-c).

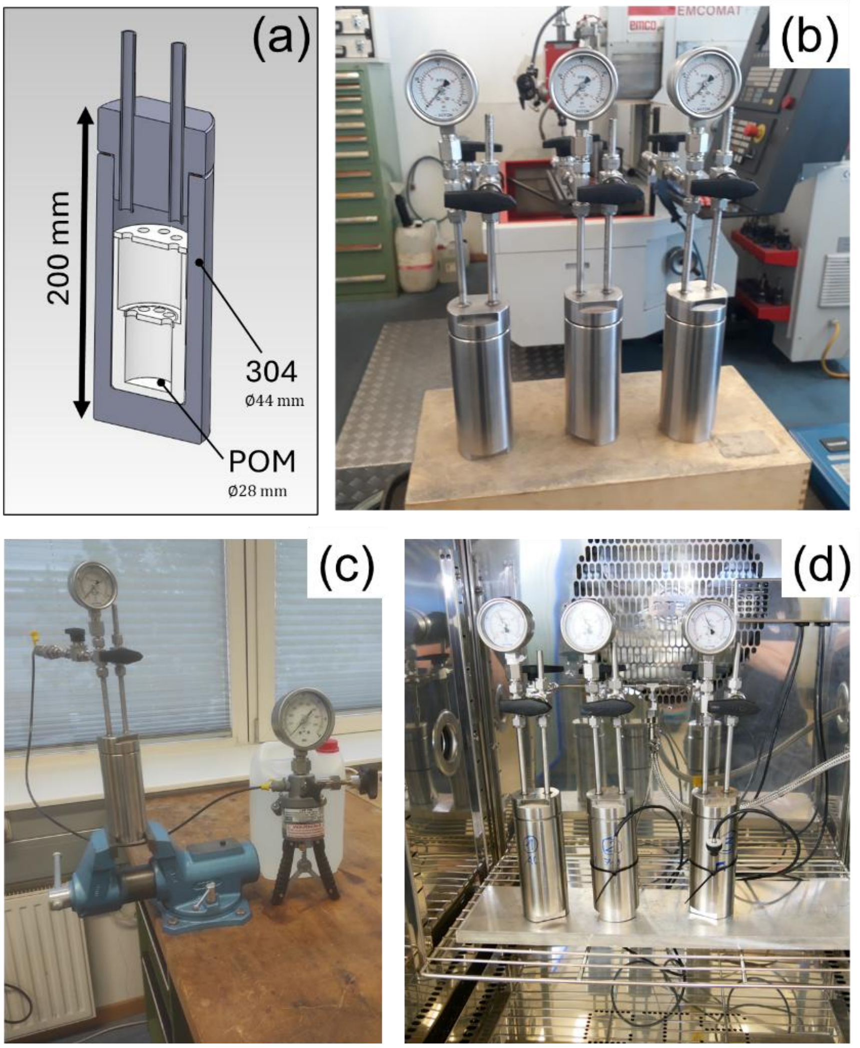

Figure 10 – Overview of the test setup for the custom-made corrosion reactors. (a) Schematics; (b) Final appearance; (c) Pressure test setup; (d) Positioning in the climate chamber

Each reactor was loaded with 03 samples of each selected material, filled halfway with water, and sealed. The reactors were then placed inside a CTS TS350 climate-controlled chamber, where the temperature was maintained at 50 °C. This temperature was monitored both by the chamber's built-in thermocouple and by an external thermocouple attached to one of the reactor walls (Figure 10-d). Gaseous CO_2 was subsequently injected into each reactor until an internal pressure of 60 bar was reached. The reactors were held under these conditions for 30 days.

Due to capacity limitations, only three materials could be tested simultaneously, resulting in a total testing period of 60 days. The selected test conditions (60 bar and 50 °C) closely resemble those typically encountered in CO_2 transportation pipelines [3,15,16]. Although a slightly higher pressure would have been preferable (70 bar), sourcing CO_2 cylinders with nominal pressures above 50 bar is challenging; once heated to 50 °C inside the reactors, the internal pressure increased to 60 bar.

After the exposure period, the samples were weighed and the values compared with their initial (pre-test) masses. The results (in terms of relative mass change) are shown in Figure 11. Among the ferrous alloys, a consistent trend of mass loss is observed when the materials are exposed to either H_2O or $H_2O + CO_2$ environments, whereas no measurable change occurs under CO_2-only conditions.

The mass loss is attributed to the mildly acidic environment generated when CO_2 dissolves in water to form carbonic acid (aqueous H_2CO_3). Under the test conditions, this acidity is sufficient to destabilize the passive film and promote iron dissolution, even in alloys classified as stainless steels [3,4]. Among the steels, 2209 exhibited the highest mass loss, particularly under the $H_2O + CO_2$ condition. However, the magnitude of this variation is small, and the results should not be interpreted as definitive evidence that 2209 is intrinsically the poorest performer.

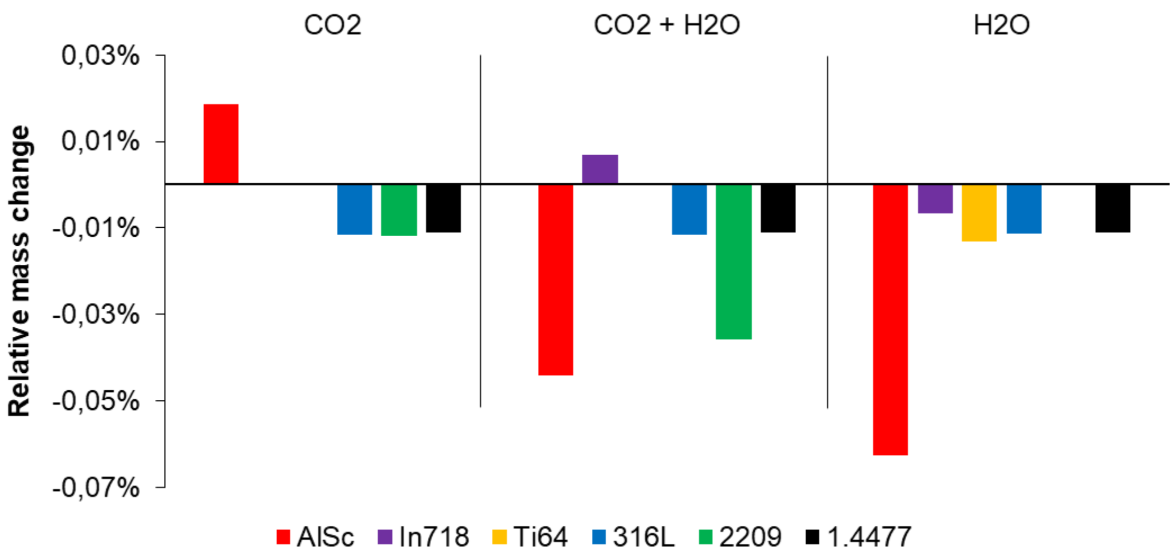

Figure 11 – Comparison of the corrosion properties of evaluated materials against different media

Among the non-ferrous alloys, mass loss was also detected and presumably for the same reasons. However, while In718 and Ti-6Al-4V show high corrosion resistance as evidenced by their low, virtually absent mass loss, the case of AlMgSc is quite clear: this material is not suitable for CO_2 transport or containment applications. With a mass loss far exceeding that of the second-worst performer (SS2209), the AlMgSc samples developed a distinctive dark surface film (Figure 12), typically associated with the formation of aluminum hydroxides and hydrated oxides resulting from passive-film breakdown in acidic CO_2-rich environments [17,18].

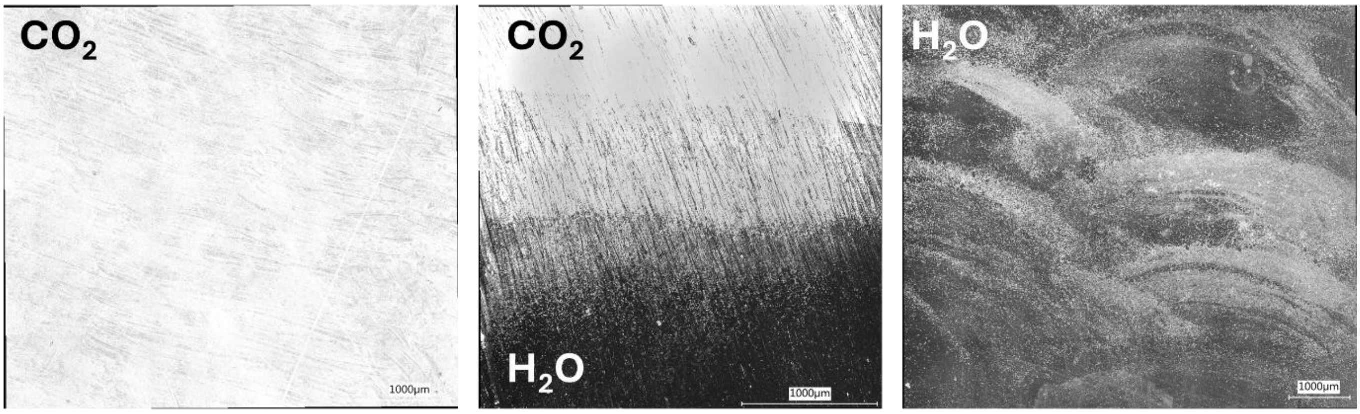

Figure 12 – Overview of surface appearance of AlMgSc placed in different media

4.6 Materials selection for demonstrator production

Due to the limited number of materials in each group, selecting the best-performing candidate did not require formal trade-off tools; the top performer in each category was evident from the results. Among the ferrous alloys, **1.4477** stood out clearly, offering the highest mechanical strength while exhibiting only minimal corrosion. The non-ferrous group required a more nuanced assessment. In principle, Ti-64 outperformed In718 in mechanical properties while showing similarly excellent corrosion resistance.

However, the RHP group already possesses extensive experience in producing and pressure-testing Ti-64 components, ranging from pressure vessels to vacuum chambers, including within previous ESA projects ("PMD4V", where the vessel withstood a pressure of 600 bar). Although this work confirms that property-wise AM Ti-64 is fully suitable for CO_2 transport and storage applications, the research team ultimately selected **In718** for the demonstrator. This choice offered a more valuable opportunity to expand knowledge and explore a material with which the group has comparatively less practical experience.

4.7 Design and Fabrication of demonstrators

The idea of the demonstration was to fulfill three aspects:

- The 3D-printed part must reflect a real-world part (e.g. pipes);
- It must have challenging features from the 3D-printing standpoint (e.g. overhangs);
- It must be integrated with a commercial component (e.g. welded to a flange or other pipe).

Based on this, two slightly different demonstrators were designed for the two selected alloys (1.4477, In718), as shown in Figure 13. Both demonstrators consist of pipes with diameter reductions and were printed in the Z-direction using a spiral-mode strategy, in which the toolpath rotates continuously at a constant angular rate while the build height increases, rather than following a layer-by-layer sequence. The reduction in cross-section created overhangs of approximately 16–17°, which at the practical limit for both selected materials based on prior experience.

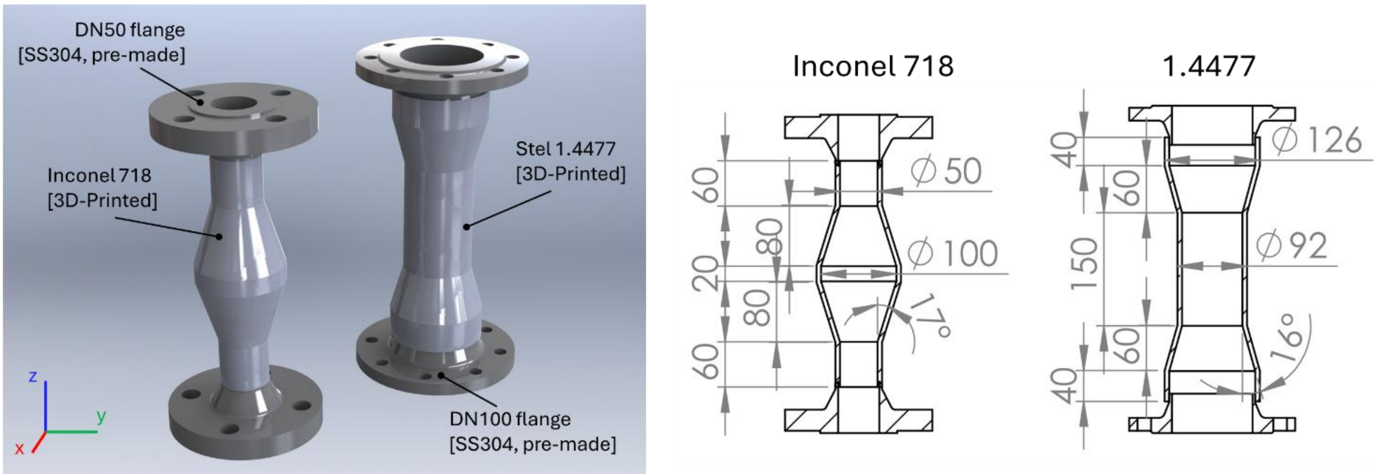

Figure 13 – Left: 3D rendering of the designed demonstrators; Right: demonstrator schematics

For the 1.4477 demonstrator, two DN100 flanges with eight bolt holes were originally planned for welding at both ends using TIG. The same approach was used for the In718 demonstrator, but with a four-hole DN50 flange. The commercial flanges selected were made of 304 stainless steel and intended to be PN100, meaning they were rated for pressures up to 100 bar. However, due to procurement constraints, PN16 flanges were used instead, which ultimately limited the maximum achievable test pressure, as discussed later.

A summary of the main aspects of the production of both demonstrators is summarized in Table . In general, Inconel 718 could be deposited at a slightly faster rate and with lower energy input than 1.4477. This behavior can be primarily attributed to the demonstrator geometry: the smaller diameters in the In718 design promoted greater heat accumulation, which in turn allowed stable melting at reduced travel speeds.

That said, additional evidence may also suggest that intrinsic material characteristics play a secondary role. For instance, the lower thermal conductivity found on In718 (11.4 W/m.K versus 14-16 W/m.k range for steels [19]) is known to enhance heat retention during processing, which could further support stable deposition under lower energy conditions. Despite being produced at twice the speed, the overall production rate remained similar to the 1.4477 demo due to a 20% lower growth per table turn, which was found to be ideal for In718.

Table 2 – Summary of process parameters and main responses concerning 3D-printing of demonstrators

Aspect	1.4477 demo	Inconel 718

		demo
As-built weight	4.66 kg	2.72 kg
Average wall thickness	6.8 mm	6.5 mm
Flange welding	Fillet welding (TIG)	Butt welding (TIG)

Following 3D printing, the demonstrators were cut from the substrate (material loss roughly estimated at 2-3%) and the respective flanges were welded on using TIG. Two welding configurations were intentionally explored: fillet welding and butt welding. This was done mainly to gain preliminary insight into how different joint types behave in this context. It should be emphasized, however, that for pressure-bearing components of this kind, butt welding is almost exclusively used in practice. Fillet welds are generally much weaker and are typically not considered suitable for high-pressure applications.

An overview of the progression of each demonstrator through the successive manufacturing steps (from printing to the final welded-flange configuration) is shown in Figure 14.

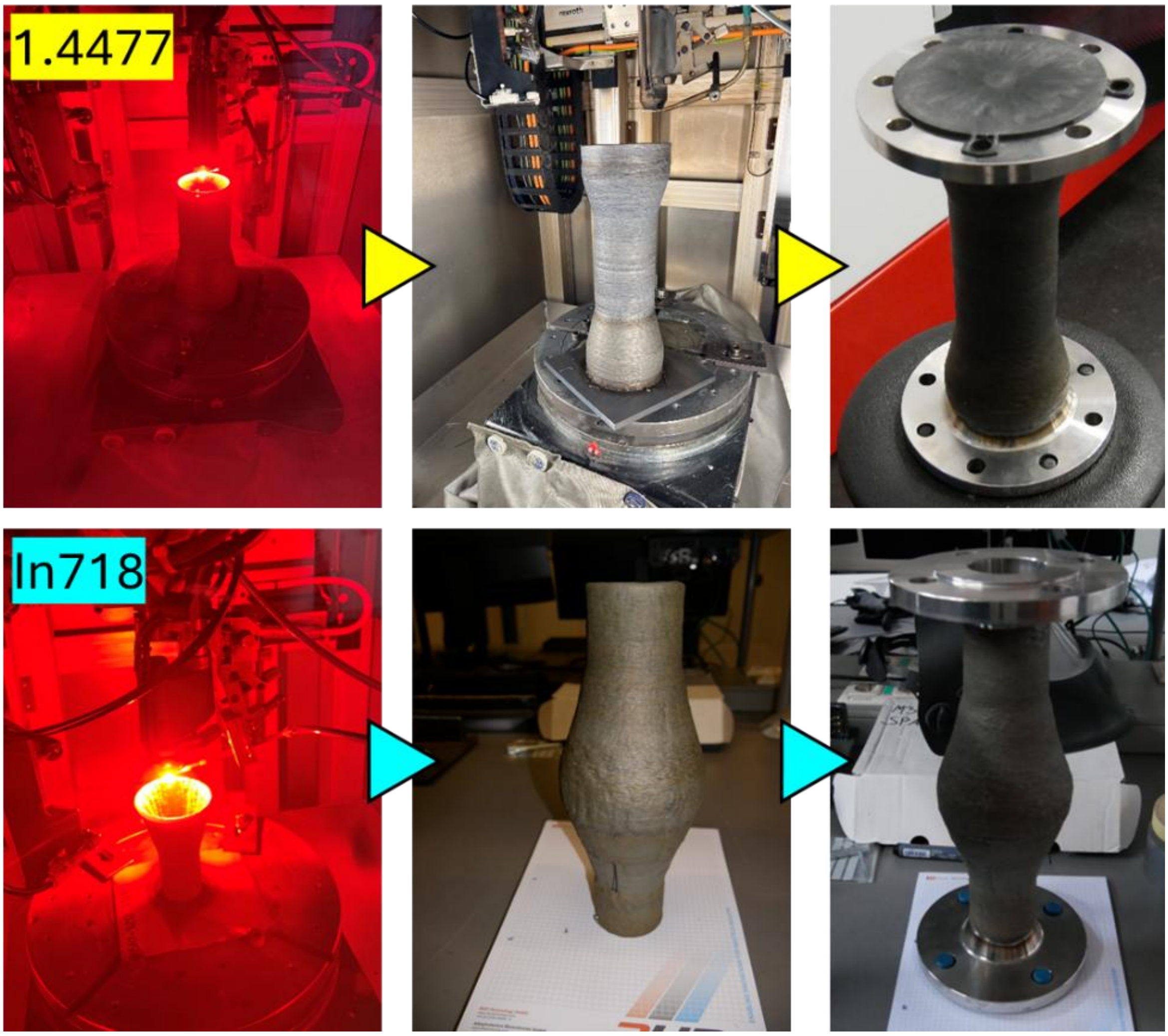

Figure 14 – Overview of manufacturing steps for each demonstrator

4.8 Pressure test of demonstrators

The pressure test was also conducted at FOTEC. Similar to the pressure test on the corrosion reactors produced in-house, the demonstrator test was carried out using water rather than CO_2, as the objective was to apply a controlled stress load to the 3D-printed walls, the flange weld seams, and the flanges themselves. Under ideal conditions, the demonstrators would have been tested at 70 bar and 50 °C, with the latter achieved by heating tapes wrapped around the printed bodies. These parameters would replicate typical CO_2 transport conditions, as illustrated in Figure 15 [16].

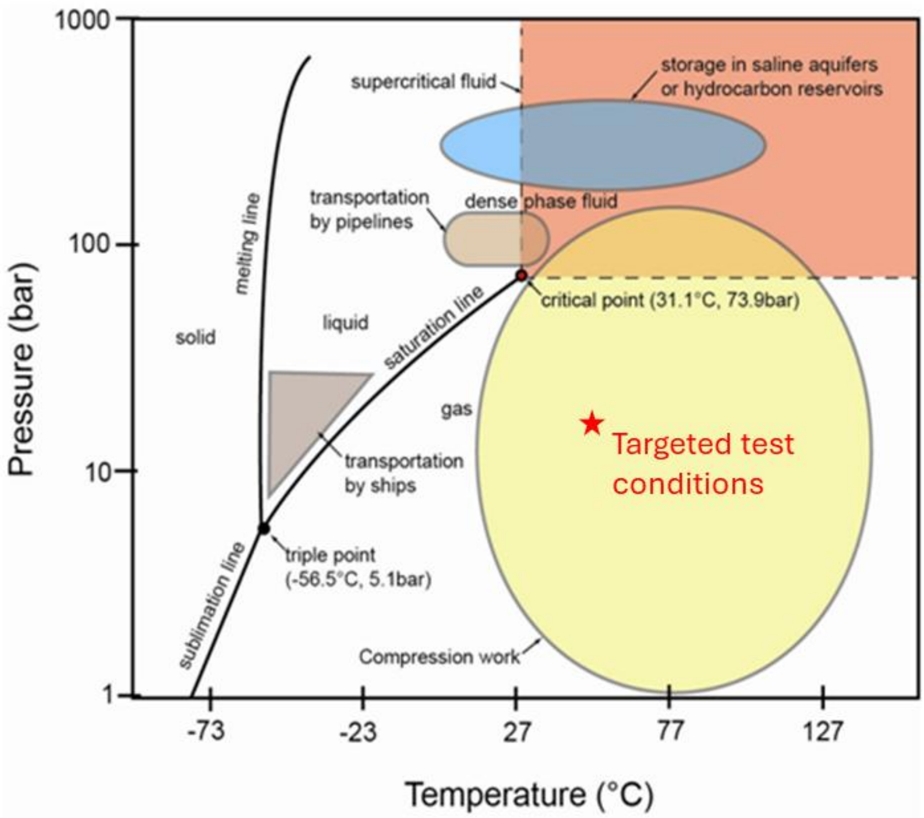

Figure 15 – Phase diagram of CO2, with regions of interested highlighted. Star denotes the test conditions

However, as noted earlier, procurement constraints meant that PN16 flanges were used instead of the intended PN100 components, making such elevated pressures unsuitable. Since water is inherently safer for pressure testing and still allows meaningful assessment of structural integrity, the test pressure was set to 20 bar—slightly above the nominal rating of the commercial flanges, but within a range that balanced safety with the need to challenge the demonstrator.

Before testing, both vessels were brought to the target temperature using heater tapes. Water was then pumped in, and pressure was monitored through a manometer mounted directly on the flanges. In both demonstrations, failure occurred before the specified pressure was reached, consistently initiating along the weld regions (see Figure 16). The In718 vessel failed slightly above 1 bar, indicating that the dissimilar-material joint requires further metallurgical improvement. The 1.4477 vessel failed near 17 bar, with leakage insufficient to counteract the inlet pressure; in this case, the weld process itself needs tighter control to avoid local material deficits.

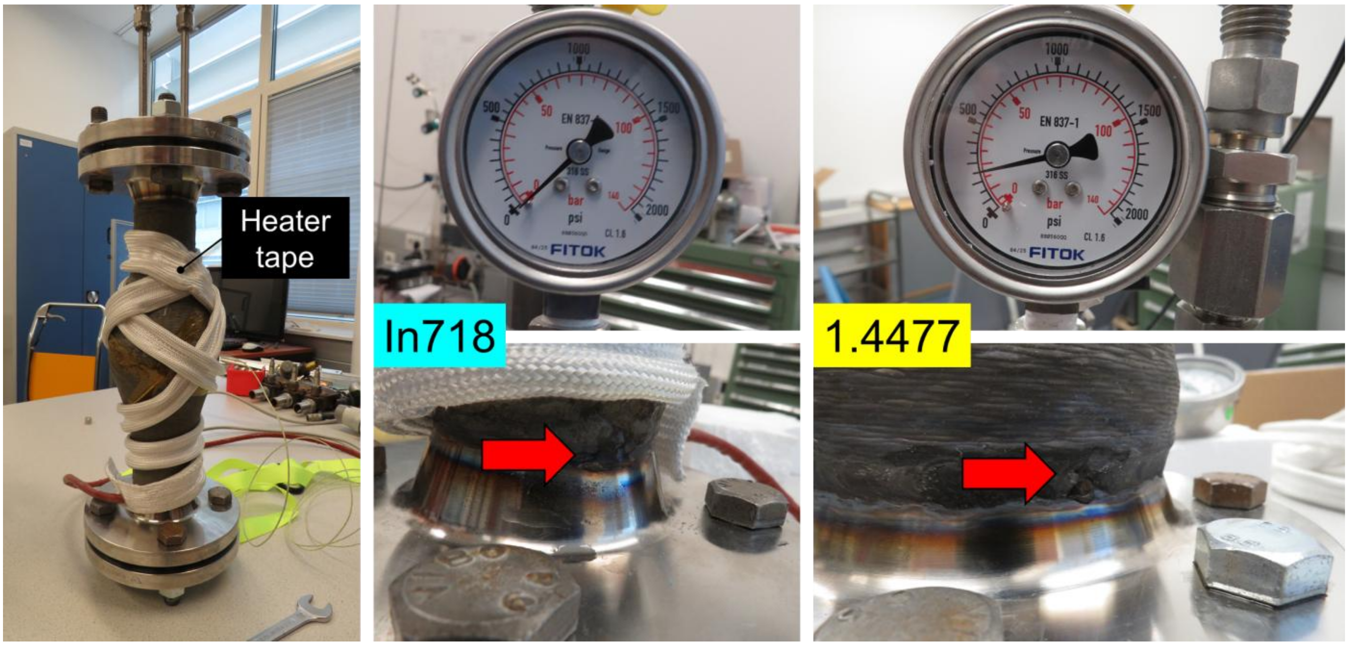

Figure 16 – Summary of the pressure test on both demonstrators using water. Red arrows indicate leakage spots, which are mainly located at weld seams.

4.9 Assessment of energy demand and material efficiency for plasma-DED vs. conventional manufacturing

This section evaluates in a virtual fashion the sustainability potential of PMD for producing complex CO_2-transport components. To quantify the environmental implications, the comparison will be done between plasma DED and conventional manufacturing routes, e.g. casting/forging followed by machining, using representative geometry (pipe section similar to the built demonstrators). The analysis considers both direct process energy and the embodied energy of material that becomes scrap, which is a major but often overlooked contributor to environmental impact.

4.9.1 Assumptions and Representative Components

To start, an upscaled version of the CO_2-transport demonstrators is here considered:

>> 1 m-long straight pipe of ø200 mm, with a ø50 mm choke

Material systems (described generically):

>> Stainless steel (approx. final mass: 32 kg)
>> Inconel-type Ni-based alloy (35 kg)

These alloys were selected since (i) they exhibited good corrosion properties and (ii) they are traditionally considered cost-intensive due to machining losses and tooling requirements.

4.9.2 Energy derived from the process itself (i.e. without material considerations)

Process	**Energy expenditure (process) [kWh/kg]**		**Total energy expenditure (process, calculated) [kWh]**		**Source Notes**
	Stainless Steel	*Inconel*	*Stainless Steel*	*Inconel*	
Plasma DED	18	14	584	488	Calculated based on values from Table 2. Machine energy estimated to be about sevenfold the main energy source [20]
Casting (melting + pouring)	2.96	3.5	95	122	Steel: [21,22] Inconel: estimated by comparison (considering Tm, heat capacity and latent heat of fusion)
Machining (roughing)	17	22	3621 (213 kg removed)	5148 (234 kg removed)	Considering a 2% oversized billet and an 8:1 “buy to fly” ratio Steel: [20] Inconel: estimated 30% higher based on material properties

Machining is clearly the main energy burden, exceeding both DED and casting, and the effect is even stronger for Inconel since it is harder to cut. The high — and in this case conservative — buy-to-fly ratio forces large amounts of material removal, which drives energy use more than any other step. This makes machining clear energy bottleneck.

4.9.3 Material Input and Scrap Generation

Assumptions:

- Plasma DED: **≈1.05x final mass (i.e. 5 % overbuild)** [own estimation]
- Casting: **≈2× final mass** [23]
- Machining route: **≈8× final mass** [20,24]

It is important to note that this comparison does not include the additional material streams consumed in conventional casting routes, such as sand for molds, binders, wax patterns, ceramic shells, gating systems, or disposable cores. These materials are typically single-use, require their own processing energy, and generate further waste that must be reclaimed or discarded. By excluding these auxiliary material flows, the assessment is conservative: it understates the total resource demand of conventional manufacturing and therefore does not fully capture the additional environmental burden associated with mold-making and foundry consumables.

4.9.4 Embodied Energy of Scrap Material and Combined Energy Comparison *(Process energy + scrap embodied energy)*

Embodied energy values per selected material (primary production):

Alloy	Embodied Energy [kWh/kg]	Source Notes
Stainless Steel	22.5	Mid interval reported for 316L [25]
Inconel	85	Mid interval reported for In718 [26]

Therefore, the embodied energy lost as scrap, as well as the TOTAL energy expenditure (combining both manufacturing process and material loss) can be calculated as follows:

	TOTAL embodied energy (material loss) [kWh]		**TOTAL energy expenditure (process + scrap) [kWh]**	
Route	*Steel*	*Inconel*	*Steel*	*Inconel*
Plasma DED	36	148	620	636
Casting	717	2962	812	3 084
Machining	5 020	20 735	8 641	25 884

Across routes, total energy demand decreases substantially when switching from casting or machining to DED. For steel, using DED instead of casting reduces total energy by roughly 25%, and by about 80% compared to machining. For Inconel, the contrast is even stronger: DED lowers total energy by roughly 80% relative to casting and around 98% relative to machining. These differences mainly reflect DED's higher material efficiency and lower scrap-related embodied energy, rather than an absence of process energy. In this sense, DED effectively enables the use of high-cost engineering alloys, as its low material losses keep total manufacturing energy substantially lower than conventional routes.

Finally, it is important to emphasize that this model has limitations and works based on approximate values present in literature. Moreover, a straight pipe can of course be produced efficiently by other conventional methods such as forming; we use it here simply as a conservative reference geometry that matches the demonstrator already built.

Since this example does not fully exploit the design freedoms of AM, any material-efficiency gains observed in this baseline case are inherently understated. If even such a simple shape shows a meaningful reduction in total energy demand, the advantage will only grow for genuinely complex components. This framing allows us to remain cautious in our claims while still illustrating the underlying trend.

5 Ausblick und Empfehlungen

5.1 Collaboration with end-users

Over the course of the project, meetings were held with representatives from at least one potential end user from the field of oil & gas, during which partial project results were presented. Particular interest was expressed in the findings related to steels. Although their current focus is on oil and gas transportation and storage, this is one of the areas where the results obtained in this project can be directly applied.

5.2 Planned events, open days and exposure

One of the demonstrators (1.4477) was 3D-printed as a showcase of the PMD technique during the RHP Open Days 2025, which over the course of three days attracted hundreds of people from several companies and places around Austria and Europe. Moreover, being a well-known marketing strategy at the RHP Group, the demonstrators generated by this project will be taken around Europe to be exhibited in the company booth during fairs and conferences.

5.3 Suggestions for future work

Based on the results of this project, the proposed follow-up activities focus on further improving hybrid manufacturing approaches for pressure-related applications. Key aspects include optimizing the joining of additively manufactured and commercial components, assessing performance under relevant pressure conditions, refining the design of testing equipment, and advancing the fabrication of more complex geometries.

6 Literaturverzeichnis

1. Cost Modelling of Additive Manufacturing/ 3D-Printing Technologies. | LinkedIn Available online: https://www.linkedin.com/pulse/cost-modelling-additive-manufacturing-3d-printing-shubham-saxena/ (accessed on 8 March 2024).
2. Directorate-General for Research and Innovation (European Commission); Brauer, H; Cooper, R; Di Biagio, Massimo; Erdelen-Peppler, Marion; Jäger, S; Kalwa, C; Kassel, C; Saysset, S; Spinelli, C. M; et al. *Requirements for Safe and Reliable CO2 Transportation Pipeline (SARCO2): Final Report*; Publications Office of the European Union, 2017; ISBN 978-92-79-77023-4.
3. Clark, B.; Rentz, R.; Mccolskey, J.; Sowards, J. *Preliminary Results from the NIST Supercritical Carbon Dioxide Corrosion Test Facility*; 2017;
4. Cheng, Y.; Bai, Y.; Tang, S.; Zheng, D.; Li, Z.; Liu, J. Corrosion Behavior of X65 Steel in CO2-Saturated Oil/Water Environment of Gathering and Transportation Pipeline. *Anti-Corros. Methods Mater.* **2019**, *66*, 671–682, doi:10.1108/ACMM-02-2019-2081.
5. Ariza Galván, E.; Montealegre-Meléndez, I.; Arévalo, C.; Perez-Soriano, E.; Neubauer, E.; Kitzmantel, M. Plasma Metal Deposition for Metallic Materials. In; 2021 ISBN 978-1-83962-820-7.
6. Committee, A.I.H. *Metals Handbook Desk Edition 2nd Edition*; Davis, J.R., Ed.; 2nd Edition.; CRC Press: Materials Park, Oh, 1998; ISBN 978-0-87170-654-6.
7. Gunn, R. *Duplex Stainless Steels: Microstructure, Properties and Applications*; Woodhead Publishing: Cambridge, England, 1997; ISBN 978-1-84569-877-5.
8. Zhang, Y.; Zou, D.; Wang, X.; Li, Y.; Jiang, Y.; Zhang, W.; Tong, L. Influence of Cooling Rate on δ-Ferrite/γ-Austenite Formation and Precipitation Behavior of 18Cr–Al–Si Ferritic Heat-Resistant Stainless Steel. *J. Mater. Res. Technol.* **2022**, *18*, 1855–1864, doi:10.1016/j.jmrt.2022.03.060.
9. Bott, I.; Souza, L.; Olaya-Luengas, L.; Valencia Morales, E. *Austenite Transformation in Duplex Stainless Steels under Fast Cooling Rates*; 2019; p. 1017;.
10. *Titanium*; Engineering Materials, Processes; Springer: Berlin, Heidelberg, 2007; ISBN 978-3-540-71397-5.
11. *Microstructural Characterization of Inconel 718 and B-1914 Superalloys: INCONEL-718 and B-1914 Nickel-Based Superalloys: Characterization and Validation of the Thermodynamic Database*; S.l., 2025; ISBN 978-620-8-66735-1.
12. Xiaogang, Y.; Tan, Y.; Cui, H.; Zhang, H.; Zhuang, X.; Zhao, L.; Niu, S.; Li, Y.; Li, P. Microstructure Evolution of an Inconel 718 Alloy Prepared by Electron Beam Smelting. *Mater. Charact.* **2021**, *173*, 110925, doi:10.1016/j.matchar.2021.110925.
13. Sawtell, R.R.; Jensen, C.L. Mechanical Properties and Microstructures of Al-Mg-Sc Alloys. *Metall. Trans. A* **1990**, *21*, 421–430, doi:10.1007/BF02782422.
14. Hua, Q.; Wang, W.; Li, R.; Zhu, H.; Lin, Z.; Xu, R.; Yuan, T.; Liu, K. Microstructures and Mechanical Properties of Al-Mg-Sc-Zr Alloy Additively Manufactured by Laser Direct Energy Deposition. *Chin. J. Mech. Eng. Addit. Manuf. Front.* **2022**, *1*, 100057, doi:10.1016/j.cjmeam.2022.100057.
15. Han, C.; Zahid, U.; An, J.; Kim, K.; Kim, C. CO2 Transport: Design Considerations and Project Outlook. *Curr. Opin. Chem. Eng.* **2015**, *10*, 42–48, doi:10.1016/j.coche.2015.08.001.
16. Paul, P., Shiladitya |. Shepherd, Richard |. Woollin Selection of Materials for High Pressure CO2 Transport Available online: https://www.twi-global.com/technical-knowledge/published-papers/selection-of-materials-for-high-pressure-co2-transport.aspx (accessed on 25 February 2026).
17. Li, D.; Shi, Z.; Xu, H.; Chen, Y.; Feng, W.; Qiu, Z.; Liu, H.; Lv, G.; Wang, S.; Fan, Y. Corrosion Behavior of Aluminum in Carbon Dioxide Aqueous Solution at 50 oC. *Int. J. Electrochem. Sci.* **2019**, *14*, 3465–3476, doi:10.20964/2019.04.47.
18. Cao, S.X.; Zhu, M.; Yuan, Y.F.; Guo, S.Y. The Influence of HCO3− Concentration on the Corrosion Resistance of 6061 Aluminum Alloy in NaCl Solution. *J. Mater. Eng. Perform.* **2025**, *34*, 14987–14996, doi:10.1007/s11665-024-10225-y.
19. Sweet, J.N.; Roth, E.P.; Moss, M. Thermal Conductivity of Inconel 718 and 304 Stainless Steel. *Int. J. Thermophys.* **1987**, *8*, 593–606, doi:10.1007/BF00503645.
20. Energy Consumption in Metal Additive Manufacturing | Digital Alloys. *digitalalloys.com*.

21. Bekker, A.C.M.; Verlinden, J.C. Life Cycle Assessment of Wire + Arc Additive Manufacturing Compared to Green Sand Casting and CNC Milling in Stainless Steel. *J. Clean. Prod.* **2018**, *177*, 438–447, doi:10.1016/j.jclepro.2017.12.148.
22. Kermeli, K.; Deuchler, R.; Worrell, E.; Masanet, E. *Energy Efficiency and Cost Saving Opportunities for Metal Casting*; 2016;
23. Karinka, S.; Vijayan, V.; Bailkeri, N. An Empirical Relation to Predict Melting/Burning Losses in the Ductile Iron Foundry. *Mater. Today Proc.* **2021**, *46*, 2831–2834, doi:10.1016/j.matpr.2021.03.055.
24. Lacalle, L.; Lamikiz, A.; Polvorosa, R.; Fernández Valdivielso, A.; Calleja, A.; Gonzalez, H.; Artetxe, E. Optimised Methodology for Aircraft Engine IBRs Five-Axis Machining Process. *Int. J. Mechatron. Manuf. Syst.* **2016**, *9*, 385, doi:10.1504/IJMMS.2016.10003806.
25. Ahmad, N.; Enemuoh, E.U. Energy Modeling and Eco Impact Evaluation in Direct Metal Laser Sintering Hybrid Milling. *Heliyon* **2020**, *6*, e03168, doi:10.1016/j.heliyon.2020.e03168.
26. Fredriksson, C. Sustainability of Metal Powder Additive Manufacturing. *Procedia Manuf.* **2019**, *33*, 139–144, doi:10.1016/j.promfg.2019.04.018.

7 Anhang

n.a.

8 Kontaktdaten

Dr. Carlos Belei
RHP-Technology GmbH
c.be@rhp.at

Dr. Erich Neubauer
RHP-Technology GmbH
e.ne@rhp.at